

Alma Mater Studiorum Università di Bologna  
Archivio istituzionale della ricerca

Design of fin structures for phase change material (PCM) melting process in rectangular cavities

This is the final peer-reviewed author's accepted manuscript (postprint) of the following publication:

*Published Version:*

Rejane De Cesaro Oliveski, Fabio Becker, Luiz Alberto Oliveira Rocha, Cesare Biserni, Gabriel Eduardo Strohm Eberhardt (2021). Design of fin structures for phase change material (PCM) melting process in rectangular cavities. JOURNAL OF ENERGY STORAGE, 35, 1-12 [10.1016/j.est.2021.102337].

*Availability:*

This version is available at: <https://hdl.handle.net/11585/818989> since: 2021-04-19

*Published:*

DOI: <http://doi.org/10.1016/j.est.2021.102337>

*Terms of use:*

Some rights reserved. The terms and conditions for the reuse of this version of the manuscript are specified in the publishing policy. For all terms of use and more information see the publisher's website.

This item was downloaded from IRIS Università di Bologna (<https://cris.unibo.it/>).  
When citing, please refer to the published version.

(Article begins on next page)

This is the final peer-reviewed accepted manuscript of:

**Rejane De Césaró Oliveski, Fábio Becker, Luiz Alberto Oliveira Rocha, Cesare Biserni, Gabriel Eduardo Stroh Eberhardt, Design of fin structures for phase change material (PCM) melting process in rectangular cavities, Journal of Energy Storage, Volume 35, 2021, 102337, ISSN 2352-152X.**

The final published version is available online at:

<https://doi.org/10.1016/j.est.2021.102337>

#### Terms of use:

Some rights reserved. The terms and conditions for the reuse of this version of the manuscript are specified in the publishing policy. For all terms of use and more information see the publisher's website.

*This item was downloaded from IRIS Università di Bologna (<https://cris.unibo.it/>)*

***When citing, please refer to the published version.***

# DESIGN OF FIN STRUCTURES FOR PHASE CHANGE MATERIAL (PCM) MELTING PROCESS IN RECTANGULAR CAVITIES

Rejane De Césaró Oliveski<sup>1</sup>, Fábio Becker<sup>1</sup>, Luiz Alberto Oliveira Rocha<sup>1</sup>, Cesare Biserni<sup>2</sup> and Gabriel Eduardo Strohm Eberhardt<sup>1</sup>

<sup>1</sup> Mechanical Engineering Graduate Program, Universidade do Vale do Rio dos Sinos, 93022-750 São Leopoldo, Brazil

<sup>2</sup> Dipartimento di Ingegneria Industriale, Università degli Studi di Bologna, Viale Risorgimento 2, 40136 Bologna, Italy

## Abstract

The objective of this work is to analyze the lauric acid PCM melting process in a finned rectangular cavity, keeping both the PCM mass and the total fin area constant, thus changing only the fin aspect ratio. The analysis was conducted through a parametric study of 78 different fin configurations. In order to maintain the thermal capacity, the cavity and fin areas were kept constant while fin dimensions were varied within a preset number of combinations of area fraction and width. The fins tested were combinations of 9 fin aspect ratios ( $RA_f$ ) and 9 fin-to-cavity area fractions ( $\phi$ ). A finite-volume numerical CFD method was used to obtain the results. Governing equations were the conservation of mass, momentum and energy while phase change was governed by an enthalpy-porosity model. The mathematical model was validated against reference experimental results and computational meshes were checked with GCI. For all tested cases, with an increase in the fin length and a consequent reduction in  $RA_f$ , there was a reduction of the total time of the melting process. The  $RA_f$ , which had shorter melting times, were defined as optimal aspect ratios ( $RA_{opt}$ ). Thus, each  $\phi$  tested resulted in its own  $RA_{opt}$ . For  $\phi = 0.005, 0.01, 0.02, 0.03, 0.04, 0.05, 0.1, 0.2$  and  $0.3$ ,  $RA_{opt} = 0.013, 0.026, 0.052, 0.078, 0.104, 0.130, 0.260, 0.592$  and  $0.889$ , respectively. Future works could contemplate a greater number of fins, with the same total area of this study, other PCM and other temperature differences, for example.

**Keywords:** Phase Change Material (PCM). Melting process. Numerical simulation. Fin aspect ratio, area fraction.

## Nomenclature

$A_c$	cavity area, $A_c = H W$	[m <sup>2</sup> ]
$A_f$	fin area, $A_f = H_f / W_f$	[m <sup>2</sup> ]
$C$	porous zone constant	[kg m <sup>-3</sup> s <sup>-1</sup> ]
$c_p$	specific heat	[J kg <sup>-1</sup> K <sup>-1</sup> ]
$Fo$	Fourier number, $Fo = \alpha t / L_c^2$	[-]
$\vec{g}$	gravity	[m s <sup>-2</sup> ]
$H$	cavity height	[mm]
$h$	heat transfer coefficient	[W m <sup>-2</sup> K]

38	$k$	thermal conductivity	[W m <sup>-1</sup> K <sup>-1</sup> ]
39	$L$	latent heat	[J kg <sup>-1</sup> ]
40	$L_c$	characteristic length, ( $L_c = A_c^{1/2}$ )	[mm]
41	$Nu$	Nusselt number, $Nu = h L_c / k$	[-]
42	$p$	pressure	[Pa]
43	$q''$	heat flux	[W m <sup>-2</sup> ]
44	$RA$	aspect ratio, $AR = H / W$	[-]
45	$\vec{S}$	momentum equation source term	[Pa m <sup>-1</sup> ]
46	$T$	temperature	[K]
47	$t$	time	[s]
48	$\vec{V}$	velocity vector	[m s <sup>-1</sup> ]
49	$W$	cavity width	[mm]
50	$W_f$	fin width	[mm]
51			
52	<i>Greek symbols</i>		
53	$\beta$	liquid fraction	[-]
54	$\varepsilon$	computational constant	[0,001]
55	$\lambda$	specific enthalpy	[J kg <sup>-1</sup> ]
56	$\mu$	dynamic viscosity	[kg m <sup>-1</sup> s <sup>-1</sup> ]
57	$\rho$	density	[kg m <sup>-3</sup> ]
58	$\phi$	area fraction, $\phi = A_f / A_c$	[-]
59			
60	<i>Subscripts</i>		
61	$c$	cavity	
62	$f$	fin	
63	$i$	initial	
64	$L$	phase change	
65	$l$	liquid	
66	$m$	melting	
67	$opt$	optimal	
68	$ref$	reference	

69	<i>s</i>	solid
70	<i>se</i>	sensible
71	<i>w</i>	wall

## 72 1. INTRODUCTION

73           The increase in energy demand, air pollution, energy prices, partial unavailability of fossil  
74 fuels and environmental concerns are driving causes of studies on alternative methods of energy  
75 production (Reddy, Mudgal, and Mallick 2018). As an extension, the development and application of  
76 energy storage techniques has become a crucial part of this area. Among the different forms of energy  
77 storage, thermal storage through sensible, latent or thermochemical heat (Zhang et al. 2016) has  
78 become one of the most used in several applications (Hasnain 1998; Dabiri, Mehrpooya and Nezhad  
79 2018; Zhu, Ma, and Wang 2009). The latent heat technique has become more attractive due to its  
80 high energy storage capacity and the ability to provide heat at a constant temperature equal to the  
81 material transition temperature. The materials used in latent heat energy storage are called Phase  
82 Change Materials (PCM) (Ibrahim et al. 2017). These are classified according to their chemical  
83 composition into organic (paraffin and non-paraffin), inorganic (salt and metal hydrates), and eutectic  
84 (metal alloys) (Jamil et al., 2019, Ibrahim et al., 2017). As for the phase change temperature  
85 classification, three groups are universally accepted: low, medium, and high temperature, Ehms et  
86 al., 2019. According to Pielichowska et al., (2014), PCM is considered low temperature when the  
87 phase change occurs at up to 15 °C, medium temperature when the phase change should occur  
88 between 15 °C and 90 °C, and high temperature when the phase change occurs above 90 °C.

89           The selection of a PCM depends on its thermal properties, applications, stability and cost  
90 (Aslfattahi et al., 2020). Their application can occur in many areas such as biomedicine, textile,  
91 automotive (Jaguemont et al., 2018) and construction (Pielichowska and Pielichowski 2014,  
92 Souayfane et al. 2016), solar power plants (Zhang et al. 2016, Khan et al. 2017) and electronic  
93 components (Baby e Balaji 2012, Kalbasi and Salimpour, 2015). In buildings, PCM can be used for  
94 cooling in passive or active systems (Souayfane et al. 2016). For example, one way of using PCM in  
95 buildings is through the inclusion of micro-encapsulated PCM in the materials used in construction  
96 (Kalnaes et al., 2015). Another interesting application of PCM is in the temperature control of electric  
97 car batteries. In this case, according to Jaguemont et al. (2018), PCM should have a melting point  
98 between 45 °C and 50 °C to obtain greater efficiency. Solar absorption refrigeration systems can also  
99 use PCM adapted to the working temperature, mass rate and loading and unloading time (Khan et al.  
100 2017). Another interesting application refers to the use of PCM as thermal protection for food

101 products sensitive to thermal variations (Leducq et al. 2015). In terms of cooling electronic  
102 components, Baby e Balaji (2012) studied experimentally the application of PCM with different types  
103 of fins and at different power levels. It was found that, by including PCM in the finned cavity, the  
104 electronic device showed a significant improvement in operating time.

105         PCMs have several advantages: small volumetric variation during phase change processes,  
106 high specific heat and latent melting heat (Baby and Balaji 2012) as well as thermal stability  
107 (Jaguemont et al. 2018). On the other hand, these materials have characteristic low thermal  
108 conductivities which result in low charge and discharge rates (Akeiber et al. 2016; Pizzolato et al.  
109 2017). Therefore, it is necessary to incorporate additional techniques to improve heat transfer between  
110 the cavity and PCM. Among these techniques there are: multiple PCM usage (Ibrahim et al. 2017),  
111 high thermal conductivity particle dispersion in the PCM (Wu et al. 2020), microencapsulation (Sun  
112 et al. 2019) and fins. According to Kean et al. (2018), the inclusion of nanoparticles can reduce the  
113 time of the melting or solidification processes. But, if nanoparticle concentration is in excess, a  
114 negative effect may occur due to the agglomeration of material. In terms of thermal and enthalpic  
115 stability with nanoparticle PCM, Aslfattahi et al. (2019) found an increase in thermal stability as well  
116 as a decrease in melting point, compared to pure material.

117         Baby and Balaji (2012) studied experimentally the application of PCM to cool electronic  
118 components. Different types of fins were investigated at different power levels. It was found that, by  
119 including PCM in the finned cavity, the electronic device showed a significant improvement in  
120 operating time. In general, fins result in an increase in active area and promote natural convection and  
121 associated thermal processes such as phase change. Consequently, the natural convection process is  
122 a defining parameter in the efficiency of finned systems. Fin geometry and positioning are also  
123 important to the phase change process (Kazemi et al. 2018; Pu et al. 2020; Abdulateef et al. 2017). In  
124 tubular systems, longitudinal fins placed at the bottom of the cavity allowed the formation of  
125 recirculation zones which decreased PCM melting time (Kazemi et al. 2018). In comparison, tubular  
126 systems with radial fins were also studied with variations in height and number of fins while keeping  
127 the volume fraction and thickness constant (Pu et al. 2020). In this case it was determined that  
128 configurations with longer fins decreased natural convection, reduced fin interactions and increased  
129 melting time but an intermediate length was deemed the most adequate. Triple tube cavities were  
130 studied with different configurations of rectangular and triangular fins (Abdulateef et al. 2017).  
131 Results showed that placement of the fins affected substantially natural convection and could reduce  
132 total melting times.

Several different fin geometric characteristics can be varied to evaluate their effect in PCM melting. In the case of varying fin thickness in rectangular cavities, an optimum ratio of fin thickness to combined fin + PCM volume which increased heat transfer rate through the fin but did not reduce considerably heat transferred from the wall to the PCM was determined (Mostafavi, Parhizi, and Jain 2019). Fin thickness was also found to be directly proportional to heat transfer through it and inversely proportional to temperature at its base, which improved cooling in the system (Arshad et al. 2020). Fins of different geometries were also examined in the melting process of paraffin PCM with or without nanoparticles (Kok 2020). In this case, fin geometries that probed into regions of un-melted PCM resulted in more satisfactory results than conventional fins despite having less heat transfer surface area. Melting lauric acid PCM was studied in rectangular cavities with 3 fins of different widths and placement (Joshi and Rathod 2019). It was determined that reducing the width of upper fins did not affect melting time but increased thermal storage capacity. Melting RT42 PCM was studied numerically in rectangular cavities with two fins with varying lengths placed at different heights while maintaining a constant total length (Ji et. al., 2018). It was proven that placement of shorter fins higher and longer fins lower reduced total melting time when compared to two fins of equal length. However, there was a limit to the length of the shorter fin, below which there were no changes to melting time. Of these, fins are the most attractive due to ease of construction and low manufacturing cost (Agyenim et al. 2010).

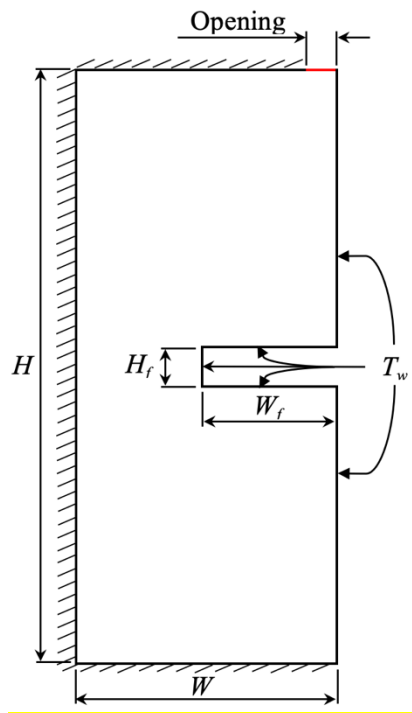
There are several studies in the literature on PCM melting/solidification in finned cavities. However, studies of this type that maintain constant total fin area and PCM mass have not been found in the literature. Thus, the objective of this study is to analyze the PCM melting process in a finned rectangular cavity keeping both the PCM mass and the total fin area constant, thus changing only the fin aspect ratio. With this, it becomes possible to determine the optimal aspect ratio to minimize the total melting time for different fractions of the area between fin and cavity.

## 2.1 Physical Domain

The studied physical domain, depicted in Fig. 1, consisted of a two-dimensional rectangular cavity with a width ( $W$ ) of 50 mm and height ( $H$ ) of 120 mm filled with lauric acid PCM initially in a solid-state. A “negative fin”, i.e. a morphing lateral intrusion, was positioned horizontally at the center of the right wall with specified width ( $W_f$ ) and height ( $H_f$ ). A 2 mm opening was located in the upper wall near the right side to simulate the loss of PCM from the cavity during the melting process. While classical fin problems with a fixed temperature at its base do result in variations of temperature

165 along the length of the fin, the physical scale of the problem results in essentially a constant-  
 166 temperature fin. This was observed in the experimental study of Kamkari and Shokouhmand 2014;  
 167 and used to validate the numerical results of Joshi and Rathod 2019. So, it also was incorporated as a  
 168 boundary condition in this work. The upper, lower, left side, front and rear walls were considered  
 169 thermally insulated. This condition guaranteed null heat flow through these walls. Furthermore, with  
 170 this condition, there was no temperature difference between the front and rear walls. Consequently,  
 171 no considerable flow or circulation was expected to develop along this direction and the physical  
 172 problem can be considered two-dimensional.

173



174

175

Figure 1 – 2D cavity domain with a morphing lateral intrusion shaped as a fin.

176

177 The constraints of the parametric study were the cavity area ( $A_c = HW$ ) and the fin area  
 178 ( $A_f = H_f W_f$ ). Area  $A_c$  was kept constant and equal to  $6,000 \text{ mm}^2$  while  $A_f$  was obtained from the area  
 179 fraction ( $\phi = A_f/A_c$ ). Nine values of  $\phi$  (0.005, 0.01, 0.02, 0.03, 0.04, 0.05, 0.1, 0.2 and 0.3) as well  
 180 as nine values of  $W_f$  (10 mm, 15 mm, 20 mm, 25 mm, 30 mm, 35 mm, 40 mm, 45 mm and 48 mm)  
 181 were selected. Through combinations of  $A_c$ ,  $\phi$ , and  $W_f$ , values of  $A_f$  and  $H_f$  were obtained and it was  
 182 possible to calculate the fin aspect ratio ( $RA_f = H_f/W_f$ ). The selected values of  $\phi$  and  $W_f$  resulted,  
 183 ideally, in 81 geometric configurations. Of these, 3 of them could not be simulated as they exceeded  
 184 the cavity dimensions and were discarded. Table 1 shows the dimensions of the remaining 78 fins.

185

Table 1 – Range of dimensions of fins tested.



		$W_f$ [mm]								
		10	15	20	25	30	35	40	45	48
$\phi = 0.005$	$H_f$ [mm]	3.00	2.00	1.50	1.20	1.00	0.86	0.75	0.67	0.63
$\phi = 0.01$		6.00	4.00	3.00	2.40	2.00	1.71	1.50	1.33	1.25
$\phi = 0.02$		12.00	8.00	6.00	4.80	4.00	3.43	3.00	2.66	2.50
$\phi = 0.03$		18.00	12.00	9.00	7.20	6.00	5.14	4.50	4.00	3.75
$\phi = 0.04$		24.00	16.00	12.00	9.60	8.00	6.86	6.00	5.33	5.00
$\phi = 0.05$		30.00	20.00	15.00	12.00	10.00	8.57	7.50	6.66	6.25
$\phi = 0.10$		60.00	40.00	30.00	24.00	20.00	17.14	15.00	13.33	12.50
$\phi = 0.20$			80.00	60.00	48.00	40.00	34.29	30.00	26.66	25.00
$\phi = 0.30$				90.00	72.00	60.00	51.43	45.00	40.00	37.50

The properties of lauric acid are shown in Tab. 2, Tab. 3 and Tab. 4. Table 2 presents the values of specific heat ( $c_p$ ), density ( $\rho$ ), temperature ( $T$ ), and latent heat ( $L$ ).

Table 2 - Properties of lauric acid (Adapted of Kamkari and Shokouhmand 2014).

Specific heat capacity solid/liquid [J/(kg K)]	2,180/2,390
Density solid/liquid [kg/m <sup>3</sup> ]	940/885
Melting temperature range [K]	316.65/321.35
Latent heat [J/kg]	187,210

Thermal conductivity ( $k$ ) and dynamic viscosity ( $\mu$ ) of lauric acid as a function of temperature were obtained by linear interpolation and are presented in Tab. 3 and 4, respectively. It is worth mentioning that regarding the nonmetallic PCMs, heat conduction mainly relies on the vibration of the crystal lattice, as addressed by Wu et al. (2020). The lattice component of thermal conductivity strongly depends on the way the molecules are arranged. More specifically, the temperature increase leads to a weakening of the atomic bonds, which in turn causes heat transfer inhibition. Thus, the mechanism mentioned above justifies the feeble reduction of thermal conductivity with the augmentation of temperature illustrated in Tab. 3.

Table 3 - Thermal conductivity of lauric acid (Shokouhmand and Kamkari 2013).

$T$ [K]	293	303	313	323	328	333	338	343
$k$ [W/(m K)]	0.161	0.159	0.158	0.145	0.143	0.142	0.139	0.138

Table 4 - Dynamic viscosity of lauric acid (Valeri and Meirelles 1997).

$T$ [K]	321.2	322	333	344	355	372	383
$\mu$ [kg/(m s)]	0.00760	0.00747	0.00542	0.00428	0.00338	0.00250	0.00210

## 2.2 Mathematical Model

The mathematical model used to represent the melting process consisted of the equations of conservation of mass, momentum and energy shown in Eq. (1-3), respectively:

$$\frac{\partial \rho}{\partial t} + \nabla(\rho \vec{V}) = 0 \quad (1)$$

$$\frac{\partial}{\partial t}(\rho \vec{V}) + \nabla(\rho \vec{V} \vec{V}) = \nabla(\mu \nabla \vec{V}) - \nabla p + \rho \vec{g} + \vec{S} \quad (2)$$

$$\frac{\partial}{\partial t}(\rho \lambda) + \nabla(\rho \vec{V} \lambda) = \nabla(k \nabla T) \quad (3)$$

where  $\vec{V}$  represents the velocity vector,  $t$  is the time,  $p$  is the pressure,  $\vec{g}$  is the acceleration of gravity,  $\vec{S}$  is the source term, and  $\lambda$  is the total enthalpy. The total enthalpy is obtained by adding the change in enthalpy associated with phase change ( $\lambda_L$ ) and sensible enthalpy ( $\lambda_{se}$ ), obtained through Eq. (4):

$$\lambda_{se} = \lambda_{ref} + \int_{T_{ref}}^T c_p dT \quad (4)$$

where  $\lambda_{ref}$  is the enthalpy at the reference temperature ( $T_{ref} = 298$  K). The enthalpy in phase change is calculated as  $\lambda_L = \beta L$ .

For the PCM melting process, an enthalpy porosity model (Voller and Prakash 1987) was used. The model treated the solid-liquid interface zone (mushy zone) as a porous zone with the source term obtained from Eq. (5):

$$\vec{S} = \frac{(1-\beta)^2}{(\beta^3 + \varepsilon)} C \vec{V} \quad (5)$$

where  $\beta$  is the liquid fraction,  $\varepsilon$  is a constant with value of 0.001 used to prevent division by zero and  $C$  is the porous zone constant. This constant depends on the morphology of the porous zone (Voller

222 and Prakash 1987). The net fraction of PCM within the phase change range is calculated from Eq.  
 223 (6):

$$224 \quad \beta = \begin{cases} 0 & \text{se } T < T_s \\ 1 & \text{se } T > T_l \\ T - T_s / T_l - T_s & \text{se } T_s < T < T_l \end{cases} \quad (6)$$

225 The boundary conditions adopted were of adiabatic left, lower and upper walls of the domain,  
 226 shown in Eq. (7-9), respectively:

$$227 \quad -k \frac{\partial T}{\partial x} \Big|_{\substack{x=0 \\ y=0-H}} = 0 \quad (7)$$

$$228 \quad -k \frac{\partial T}{\partial y} \Big|_{\substack{x=0-W \\ y=0}} = 0 \quad (8)$$

$$229 \quad -k \frac{\partial T}{\partial y} \Big|_{\substack{x=W-opening \\ y=0}} = 0 \quad (9)$$

230 while a prescribed temperature condition was applied on the right vertical wall, all fin surfaces and  
 231 the opening, as shown in Eq. (10, 11), respectively:

$$232 \quad T \Big|_{\substack{x=W \\ y=0-H}} = T_w \quad (10)$$

$$233 \quad T \Big|_{\substack{x=opening \\ y=H}} = T_a \quad (11)$$

### 234 **3 Numerical Model**

235 Numerical simulations were performed on ANSYS FLUENT® and the computational meshes  
 236 were created on ANSYS ICEM® version 18.2. In the reference experimental work of Kamkari and  
 237 Shokouhmand (2014), the liquid PCM was removed manually. In the present numerical work, this  
 238 PCM removal was modeled through the “*pressure-outlet*” boundary condition imposed on the  
 239 opening, with gauge pressure of 0 Pa and temperature of 343 K. For the pressure correction and  
 240 pressure-velocity coupling, the “*presto*” and “*simple*” criteria were adopted, respectively. The flow  
 241 was considered laminar transient with a time step of 0.1 s. In the energy and momentum equations, a  
 242 “*first-order upwind*” scheme was used. Absolute convergence criteria of  $10^{-8}$  for the energy equation  
 243 and  $10^{-5}$  for the velocity and continuity equations were adopted. Relaxation coefficients used were:

0.15 for pressure and momentum, 0.3 for density, field forces and energy and 0.2 for the liquid fraction. Intermediate values of  $k$  e  $\mu$  were obtained by linear interpolation of the data of Tab. 3 and Tab. 4. The value of  $\rho_s$  was considered constant as of Tab. 2; however, values of  $\rho_l$  were pre-set from reference (Chuah et al. 2006) according to temperature: 885 kg/m<sup>3</sup> at 321.35 K (Tab. 1), 870 kg/m<sup>3</sup> at 323 K and 862 kg/m<sup>3</sup> at 333 K. The lower, upper, and left walls of the cavity were defined as adiabatic. The right wall and the fin surfaces were kept at the heating temperature  $T_w = 343$  K. The no-slip condition was applied in all walls and the fin surfaces, except for the opening, which was considered free flow at  $T_a = 343$  K. In addition, the PCM was subjected to an initial temperature of  $T_i = 298$  K.

### 3.1 Model Validation and Mesh Test Sensitivity

#### 3.1.1 Model Validation

Numerical validation was performed with comparisons to reference experimental data (Kamkari and Shokouhmand 2014) in two ways: through liquid fraction field and with the liquid fraction profile over time. The reference study consisted of the melting process of lauric acid PCM in a similar physical domain. The experimental rectangular cavity measured 50 mm in width, 120 mm in height and 120 mm in thickness, with a fin 25 mm in width and 4 mm in height. The fin and the right wall were subjected to a constant temperature of 343 K while the remaining walls were thermally insulated. The PCM was initially at a temperature of 298 K, i.e., solid-state (Kamkari and Shokouhmand 2014).

Figure 2 shows a comparison of liquid fraction fields ( $\beta$ ) from the reference experimental study (Kamkari and Shokouhmand 2014) and the present numerical study at 10 min, 30 min and 50 min of the melting process. Figures 2(a, c, e) contain the experimental results and Figs. 2(b, d, f) the numerical results. In the numerical results, white and blue colors represent the solid-state PCM, while black and red colors represent the liquid state. As seen in Fig. 2, there is good visual agreement in the liquid fraction between both sets of results for all melting times.

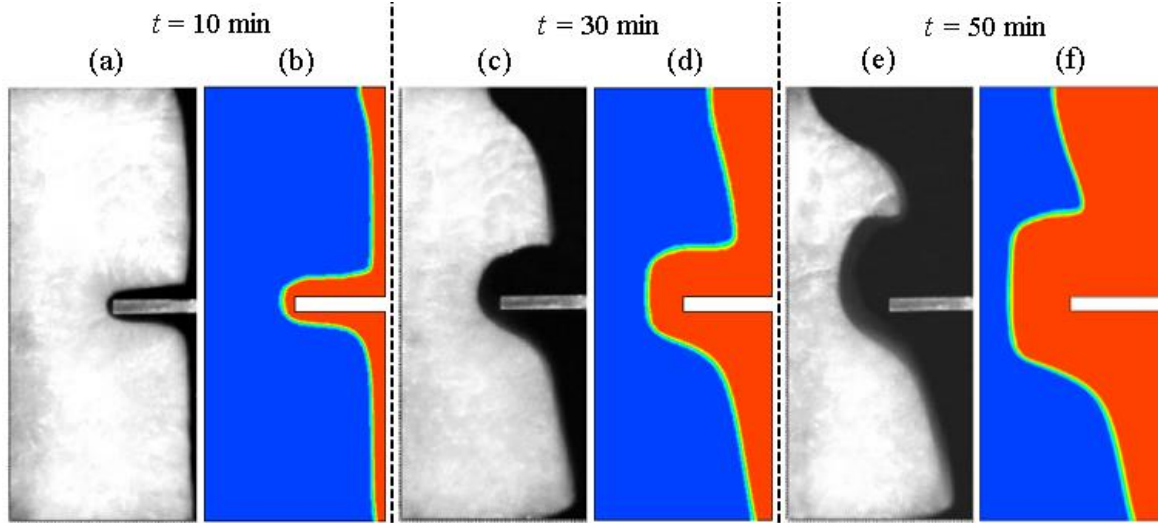


Figure 2 -  $\beta$  distribution at time  $t = 10$  min, 30 min and 50 min: (a), (c) and (e) experimental results (Kamkari and Shokouhmand 2014); (b), (d) and (f) present numerical results.

Furthermore, Fig. 3 shows transient profiles of  $\beta$  obtained experimentally (Kamkari and Shokouhmand 2014) and numerically (present study). The values of  $\beta$  range from 0 to 1, with 0 representing the solid-state PCM and 1 representing the liquid state. Coherent agreement can be clearly observed between the numerical and experimental results. The average difference was approximately 5.4%, while the maximum difference was approximately 6.3% at  $t = 110$  min with  $\beta = 0.856$ .

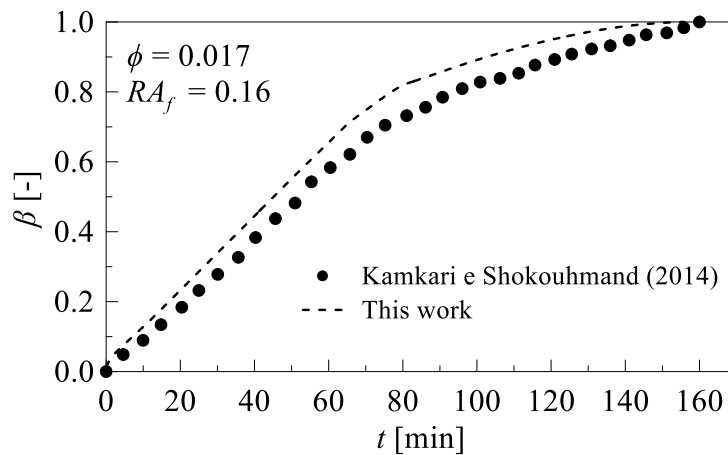


Figure 3 – Liquid fraction  $\beta$  as function of time  $t$ : comparison between experimental results (Kamkari and Shokouhmand 2014) and present numerical results.

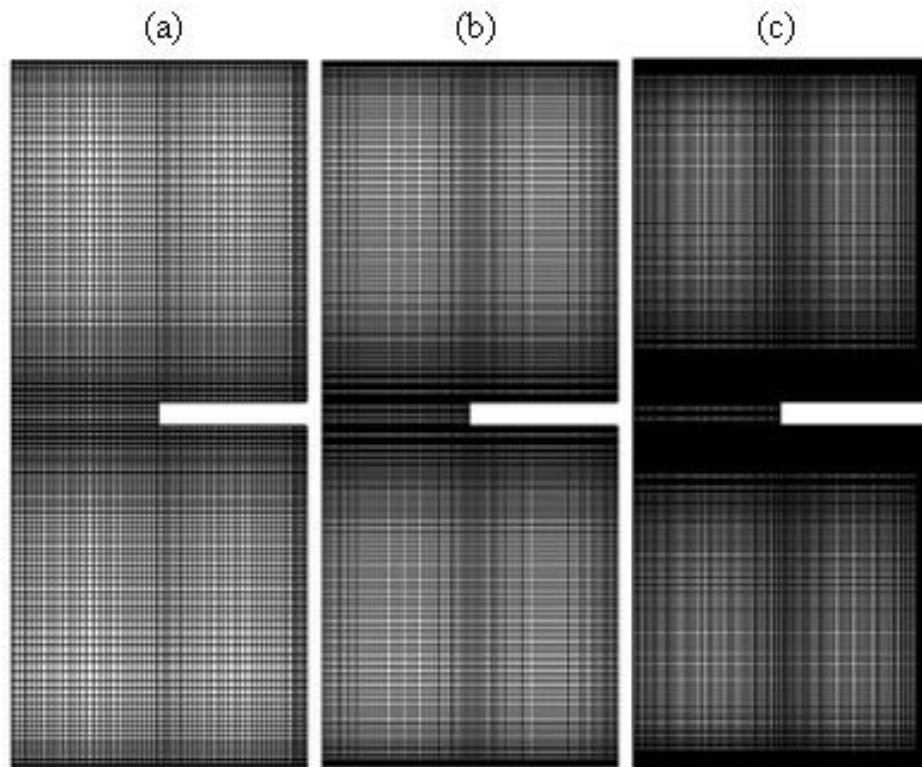
Considering the good agreement between the numerical results of the present study and reference experimental results (Kamkari and Shokouhmand 2014), both qualitative (Fig. (2)) and

285 quantitative (Fig. (3)), as well as the constant value assigned to  $C$  (seen in Section 3.1.3), the  
286 numerical model used in this study was considered validated.

287

### 288 3.1.2 Mesh Test Sensitivity

289 For the present numerical study, three computational meshes were created, as seen in Fig. 4,  
290 with increasing number of elements. Meshes (a), (b) and (c) contained 10,118, 14,520 and 28,457  
291 elements, respectively. Mesh independence analysis was performed using the GCI (Grid  
292 Convergence Method) procedure (Celik et al. 2008) by comparing the most refined mesh (c) with the  
293 intermediate mesh (b) and the least refined mesh (a). The calculated percentage rates were 1.9% and  
294 5.5%, respectively. Thus, with a GCI of 1.9%, mesh (c) with 28,457 elements mesh was considered  
295 suitable for numerical simulations.



296

297 Figure 4 – Grid convergence study meshes: (a) 10,118, (b) 14,520 and (c) 28,457 elements.

298

### 299 3.1.3 Adjustment of porous zone constant “ $C$ ”

300 The porous zone constant ( $C$ ) of Eq. (5) indicated the material velocity damping to zero in the  
301 solid phase and its value had to be adjusted according to the problem analyzed. By definition, the  
302 value of  $C$  should be sufficient to allow flow in the transition region while at the same time

303 suppressing velocity in the solid phase (Voller and Prakash 1987). For the present study, a range of  
304 several orders of magnitude of  $C$  values were tested. It was observed that a value of  $C = 10^{11}$  more  
305 satisfactorily reproduced the PCM merging process and, consequently, was kept for all the numerical  
306 results presented in this study.

307

## 308 4. RESULTS AND DISCUSSIONS

309 The objective of this study was to analyze the influence of fin aspect ratio ( $RA_f = H_f/W_f$ ),  
310 and obtain the optimal aspect ratio ( $RA_{opt}$ ), thereby minimizing the melting process time for each  $\phi$ .  
311 For clarity, each parameter affecting optimization was analyzed individually.

312

### 313 4.1 Effects of Buoyancy on the Melting Process

314 Figures 5(a, b) show the velocity fields for  $RA_f = 0.288$  and  $\phi = 0.03$  at times  $t = 20$  min and  
315 40 min, respectively. In the figures, PCM is represented with gray color in the solid phase and black  
316 color in the liquid phase, with the velocity field at the same instant of time superimposed. It can be  
317 seen in both figures that, due to the buoyancy force generated by the variation of temperature within  
318 the liquid phase, an upward flow is present close to the heated wall (right) and in the region above  
319 the fin. Downward flow can also be observed at the solid-liquid interface, thus ensuring the principle  
320 of mass conservation. In between these two convective currents and their velocity profile, it is  
321 possible to observe a shear region captured by the proper refinement of the computational mesh  
322 throughout the domain. Heating occurs along the upper side of the fin and beyond the reach of the  
323 vertical wall. In this region, a large recirculation zone is observed and can be classified as Rayleigh-  
324 Bénard convection. A similar flow can also be observed between the base of the cavity and the base  
325 of the fin, producing another recirculation zone in this region but with different characteristics.

326

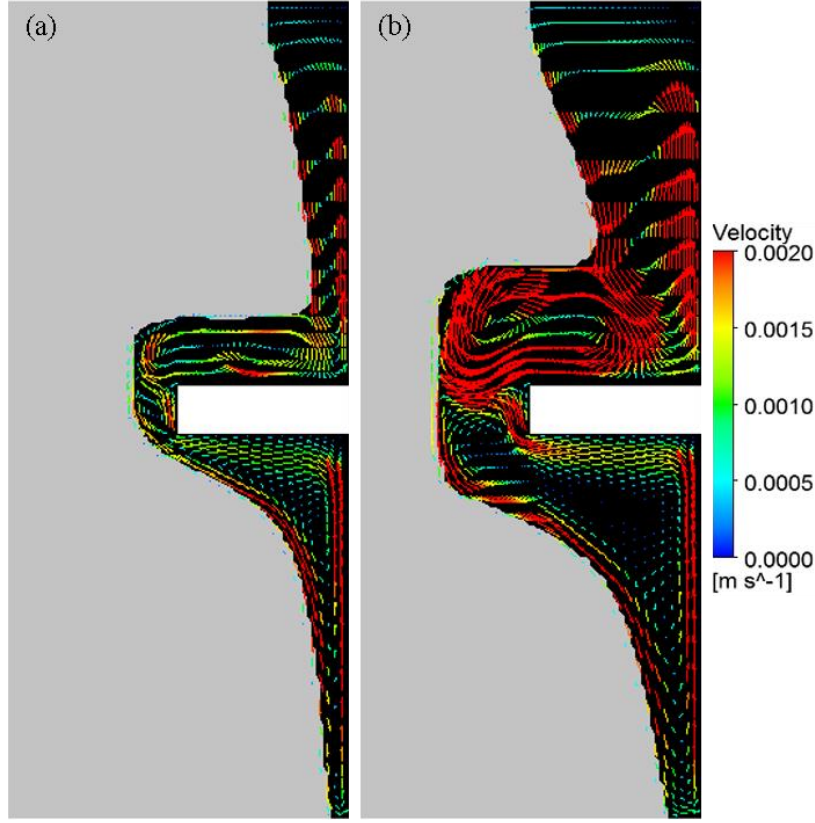


Figure 5 – Velocity distribution for  $RA_f = 0.288$  and  $\phi = 0.03$  at: (a)  $t = 20$  min, (b)  $t = 40$  min.

Figures 6(a, b) show temperature fields for  $RA_f = 0.450$  and  $0.078$  with  $\phi = 0.03$  at times  $t = 10$  min and  $50$  min, respectively. In the figures, for all presented results, a robust thermal gradient near the right vertical wall and the entire perimeter of the fin can be initially observed. Strong thermal stratification is detected in the cavity at the final  $t = 50$  min moment and especially in the region above and below the fin. Buoyant forces arising from the change in density near the active vertical wall form an upward convective current seen in Fig. 5(b). This current stratifies thermally the liquid PCM in the upper part of the cavity. A similar condition is observed below the fin for both tested values of  $RA_f$ , which contributes to the formation of a curved melting front. However, at  $t = 10$  min and  $t = 50$  min, there is an increase in thermal stratification in the region below the fin with decreasing  $RA_f$ . This behavior is related to the increase in fin perimeter, which limits the movement of the upward convective currents to the top of the cavity and contributes to accelerate the melting process. Slight temperature variations at the top of the fin at  $t = 10$  min for both tested values of  $RA_f$  have also been detected. These characteristics fused layer instabilities are associated with Rayleigh-Bénard convection formation. Finally, it is worth mentioning that, for the others tested values of area fraction  $\phi$ , this behavior is also observed.



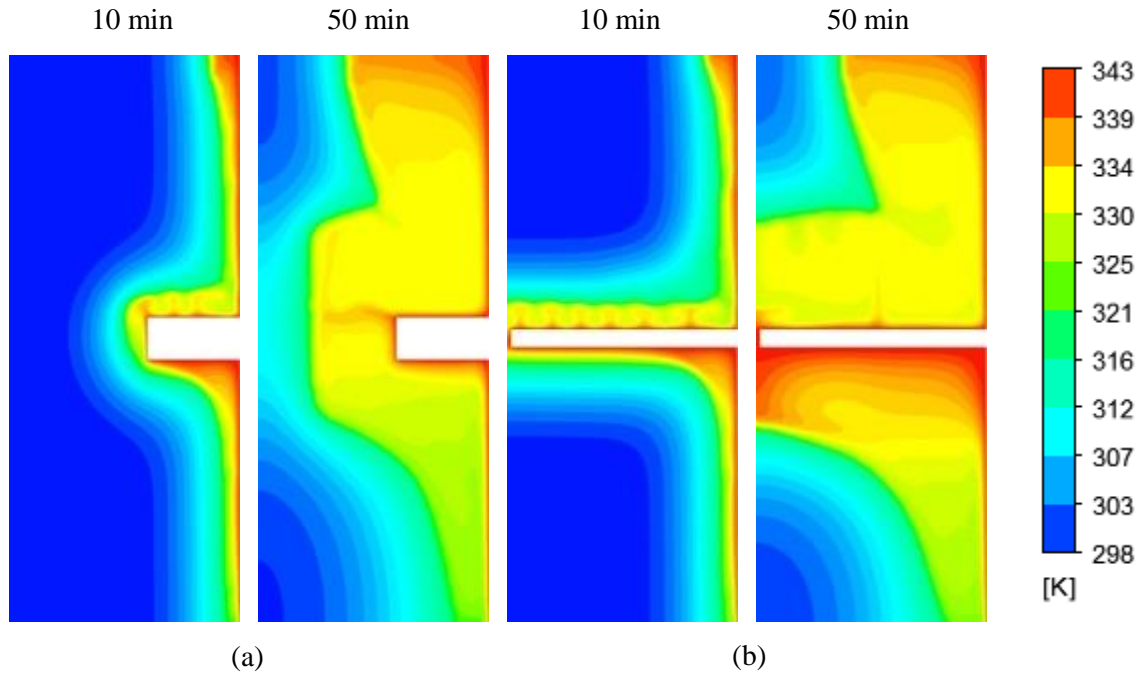


Figure 6 – Temperature distribution at  $t = 10$  and  $50$  min,  $\phi = 0.03$  and: (a)  $RA_f = 0.450$  and (b)  $RA_f = 0.078$ .

#### 4.2 Area Fraction Effect

Figures 7(a-d) show the liquid fraction ( $\beta$ ) fields at time  $t = 50$  min for  $W_f = 20$  mm and 48 mm and area fractions of  $\phi = 0.01, 0.05, 0.2$  and  $0.3$ , respectively. In the figures, the first and third columns present  $\beta$  fields with respect to the case  $W_f = 20$  mm; similarly, the second and fourth columns are with respect to  $W_f = 48$  mm. As observed in Fig. 7(a-d), there is a reduction of the total time of the melting process for any  $\phi$  with an increase in the fin width  $W_f$ , which also corresponds to a reduction in the value of  $RA_f$ . In addition, it can be seen that the liquid fraction fields near the right vertical wall are similar to each other for both  $W_f = 20$  mm and  $W_f = 48$  mm, featuring a thin layer of molten PCM for different  $RA_f$  and  $\phi$  values. It is also noted that at  $t = 50$  min and for  $\phi = 0.01$  to  $0.05$ , within different values of  $RA_f$ , the solid-liquid interface profiles are similar to each other, differing only in the region to the left of the fin between  $W_f = 20$  mm and  $W_f = 48$  mm.

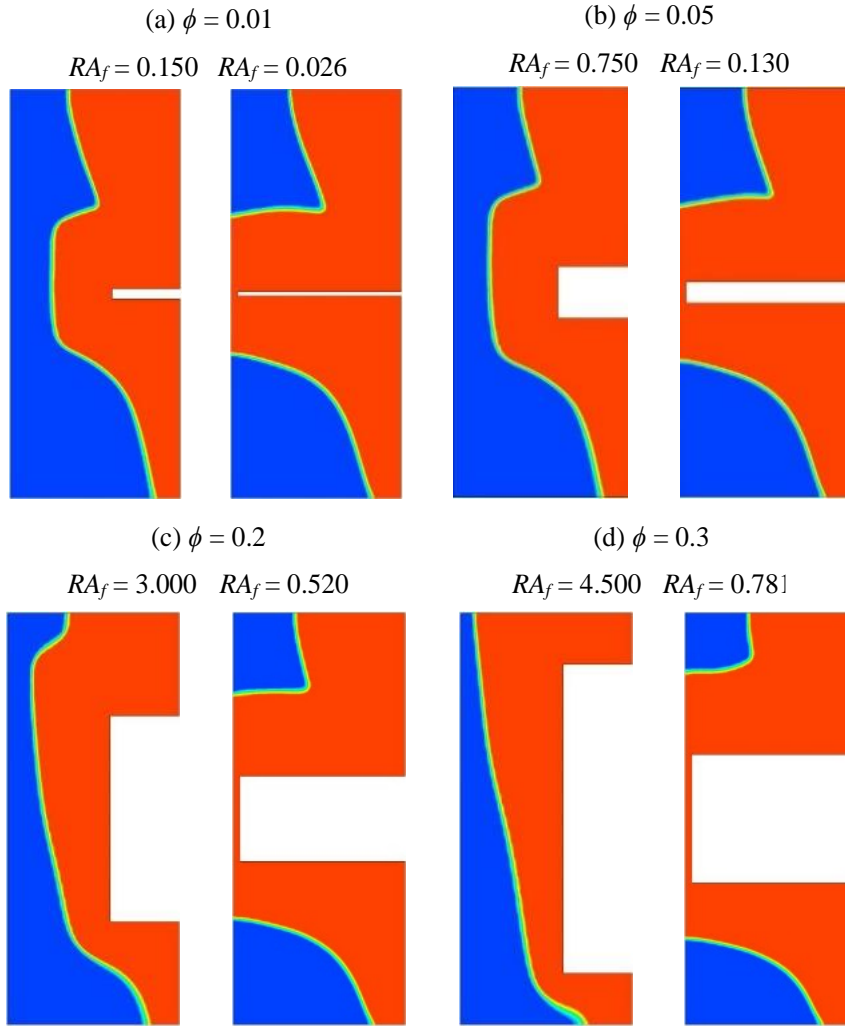


Figure 7 –  $\beta$  field at  $t = 50$  min,  $W_f = 20$  and  $48$  mm: (a)  $\phi = 0.01$ ; (b)  $\phi = 0.05$ ; (c)  $\phi = 0.2$  and (d)  $\phi = 0.3$ .

### 4.3 Effect of Fin Aspect Ratio ( $RA_f$ )

The different heat transfer mechanisms in a melting process can be identified by varying the Nusselt number ( $Nu = h L_c / k_l$ ) as a function of Fourier number ( $Fo = \alpha_l t / L_c^2$ ), where  $L_c$  is the characteristic length ( $L_c = A_c^{1/2}$ ),  $A_c$  is the cavity area,  $h$  is the heat transfer coefficient ( $h = q'' / (T_w - T_l)$ ),  $q''$  is the heat flux on the right sidewall and fin perimeter,  $T_w$  (343 K) is the wall temperature,  $T_l$  is the PCM liquid temperature and  $\alpha_l$  ( $\alpha_l = k_l / \rho_l c_{p_l}$ ) is the liquid thermal diffusivity. The heat flux ( $q''$ ) was obtained on CFX-Post from the results obtained from Fluent.

369 Figure 8(a-f) shows  $Nu$  profiles as a function of  $Fo$  for different  $RA_f$  and  $\phi = 0.01, 0.03, 0.05,$   
 370  $0.1, 0.2,$  and  $0.3,$  respectively. As seen in the figure, regardless of the values of  $RA_f$  and  $\phi$ , all results  
 371 show 3 different regions: I – with a marked reduction of  $Nu$  in the initial moments; II - with  $Nu$  values  
 372 without large variations, despite fluctuations in most of the melting process and III – a sharp reduction  
 373 of  $Nu$  in the final moments. More specifically, the low thermal resistance of the thin wall-melted  
 374 PCM layer in the initial moments allows the characterization of region I as conductive. With the  
 375 beginning of the melting process, still in region I, there is an increase in the size of the liquid layer.  
 376 This behavior induces a change in the heat transfer mechanism from conductive to convective  
 377 represented by region II. In region II,  $Nu$  continues to decrease but more slowly. This behavior is in  
 378 accordance with reference work (Ji et al. 2018) and corroborates with the observations on the velocity  
 379 fields (Fig. 5): heating at the fin tip produces recirculation of the Rayleigh-Bénard liquid PCM which  
 380 generates, in turn, fluctuations in the local temperature. Consequently,  $Nu$  also has fluctuations as  
 381 seen in region II of Fig. 8(a-f). These oscillations decrease as the solid-liquid interface moves away  
 382 from the fin in accordance with known experimental behavior (Kamkari and Shokouhmand 2014).  
 383 In addition, regarding Fig. 8(a-f), it can be observed that smaller values of  $RA_f$  ( $RA_f = H_f / W_f$ ) are  
 384 associated with longer periods of  $Nu$  fluctuations. This behavior is due to the increase of  $W_f$ .  
 385 Moreover, it is observed that increasing the value of  $\phi$  reduces the amplitude of the instabilities, which  
 386 is visually evident in a comparison of Fig. 8(a) and 8(f). This fact justifies the reduction of the time  
 387 difference of the melting process with increasing of  $\phi$  seen in the analysis of the liquid fraction  
 388 profiles. In region III, at the final moments,  $Nu$  number again decreases more sharply due to the  
 389 reduction of the heat transfer rate resulting from weakening convection currents. In this figure it can  
 390 also be observed that, for all values  $\phi$  and near  $Fo = 0.05$ , there is a small increase in  $Nu$  for the  
 391 highest  $RA_f$  values. This behavior occurs due to the greater length of the solid-liquid PCM interface,  
 392 as seen in Fig. 7(a-d). For example, in Fig. 7(a) for  $\phi=0.01$ , the length of the solid-liquid interface for  
 393  $RA_f= 0.15$  is greater than for  $RA_f= 0.026$ , resulting in a larger  $Nu$  seen in Fig. 8(a). As a final point,  
 394 it should be mentioned that for all tested  $\phi$  values, the cases with the lowest  $Nu$  are those that presented  
 395 the fastest melting processes.

396

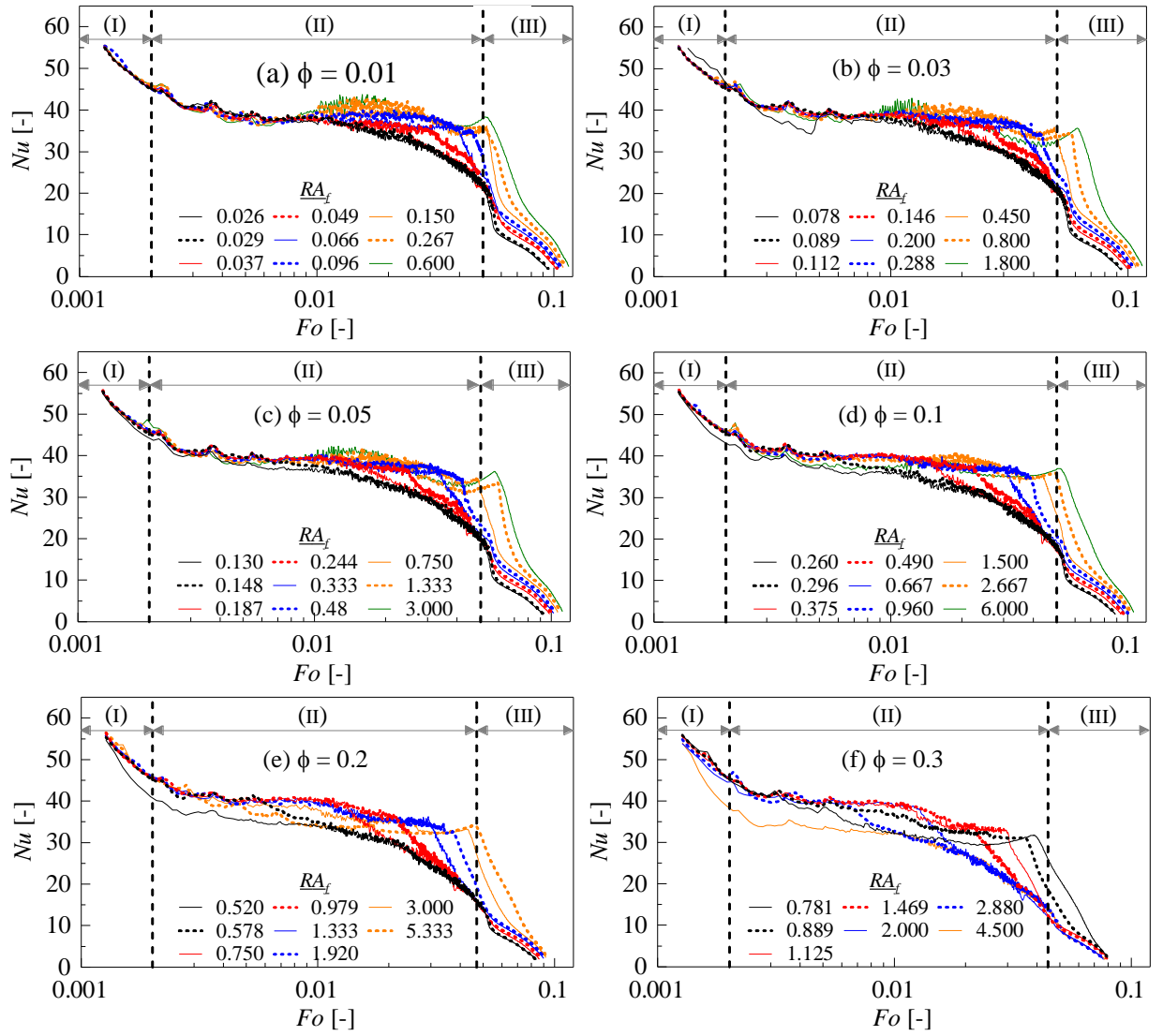
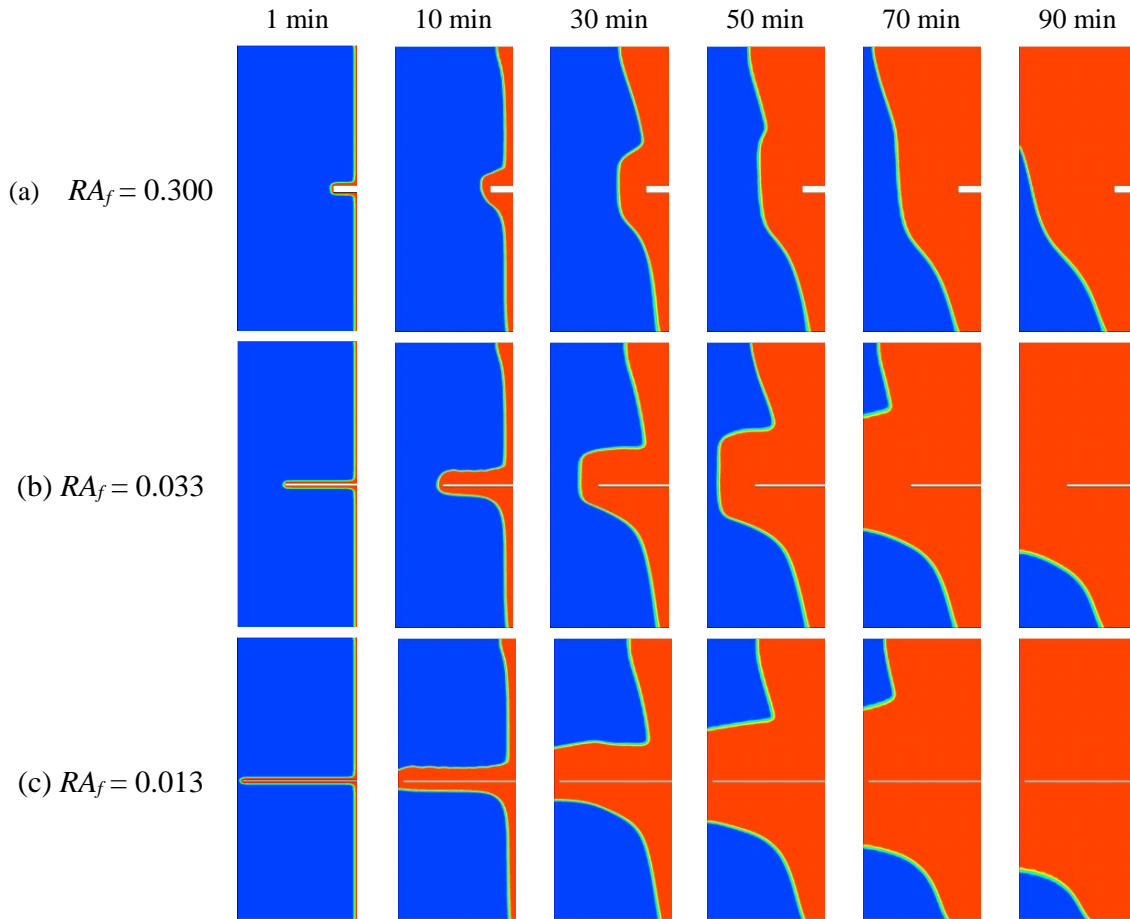


Figure 8 –  $Nu$  vs.  $Fo$ , for several values of  $RA_f$  and: (a)  $\phi = 0.01$ ; (b)  $\phi = 0.03$ ; (c)  $\phi = 0.05$ ; (d)  $\phi = 0.1$ ; (e)  $\phi = 0.2$  and (f)  $\phi = 0.3$ .

Figures 9(a-c) show  $\beta$  fields for  $\phi = 0.005$  at times  $t = 1$  min, 10 min, 30 min, 50 min, 70 min and 90 min and  $RA_f = 0.300$ , 0.033 and 0.013, respectively. As in Fig. 7, blue color represents the solid phase and red color represents the liquid phase. Initially, it is observed that at  $t = 1$  min, regardless of the values of  $RA_f$ , the fused PCM layer in the vicinity of the heated wall is very thin. At this time, the PCM is almost entirely in the solid phase and the heat transfer process is predominantly conductive. As  $t$  increases, the thickness of the molten layer increases and buoyant forces become predominant in relation to viscous ones; therefore, a change in the heat transfer mechanism occurs, becoming convective. As a result, solid-phase erosion occurs in the upper cavity at the solid-liquid interface, forming a curvature of the melting front. This can be observed in Fig 9 for all values of  $RA_f$

410 at  $t = 30$  min, 50 min and 70 min. Additionally, it is noted that  $RA_f$  also influences the melting rate.  
 411 For example, after the initial moments, there is a tendency to accelerate the PCM merger process with  
 412 reduced  $RA_f$ . This is mainly identified at  $t = 50$  min, where it can be observed that the melting rate for  
 413  $RA_f = 0.013$  is much larger than for  $RA_f = 0.3$ . This behavior is due to the augmented perimeter of the  
 414 fin inserted in the PCM, which increases the heat transfer area between the fin and the PCM.



415  
 416 Figure 9 –  $\beta$  field for  $\phi = 0.005$ ,  $t = 1$  min, 10 min, 30 min, 50 min, 70 min and 90 min, and: (a)  $RA_f = 0.300$ ;  
 417 (b)  $RA_f = 0.033$  and (c)  $RA_f = 0.013$ .  
 418

419 In quantitative terms, the influence of  $RA_f$  ( $H_f / W_f$ ) over  $\beta$  is shown in Fig. 10(a-f) which  
 420 highlights the variations of  $\beta$  as a function of time for different  $RA_f$  and  $\phi = 0.01, 0.03, 0.05, 0.1, 0.2$   
 421 and 0.3, respectively. Overall, higher values of  $RA_f$  are associated with longer complete PCM melting  
 422 times ( $\beta = 1$ ) independent of the area fraction  $\phi$ . Moreover, since the increase in  $RA_f$  leads to fins with  
 423 smaller heat exchange area, the heat removal (per unit time) process ends up being penalized.  
 424 Conversely, it can be demonstrated that there is a gradual tendency of acceleration of the melting  
 425 process with the gradual reduction of the aspect ratio  $RA_f$  for all tested values of  $\phi$ , even if it is not  
 426 evident which were the smallest calculated  $RA_f$  values.

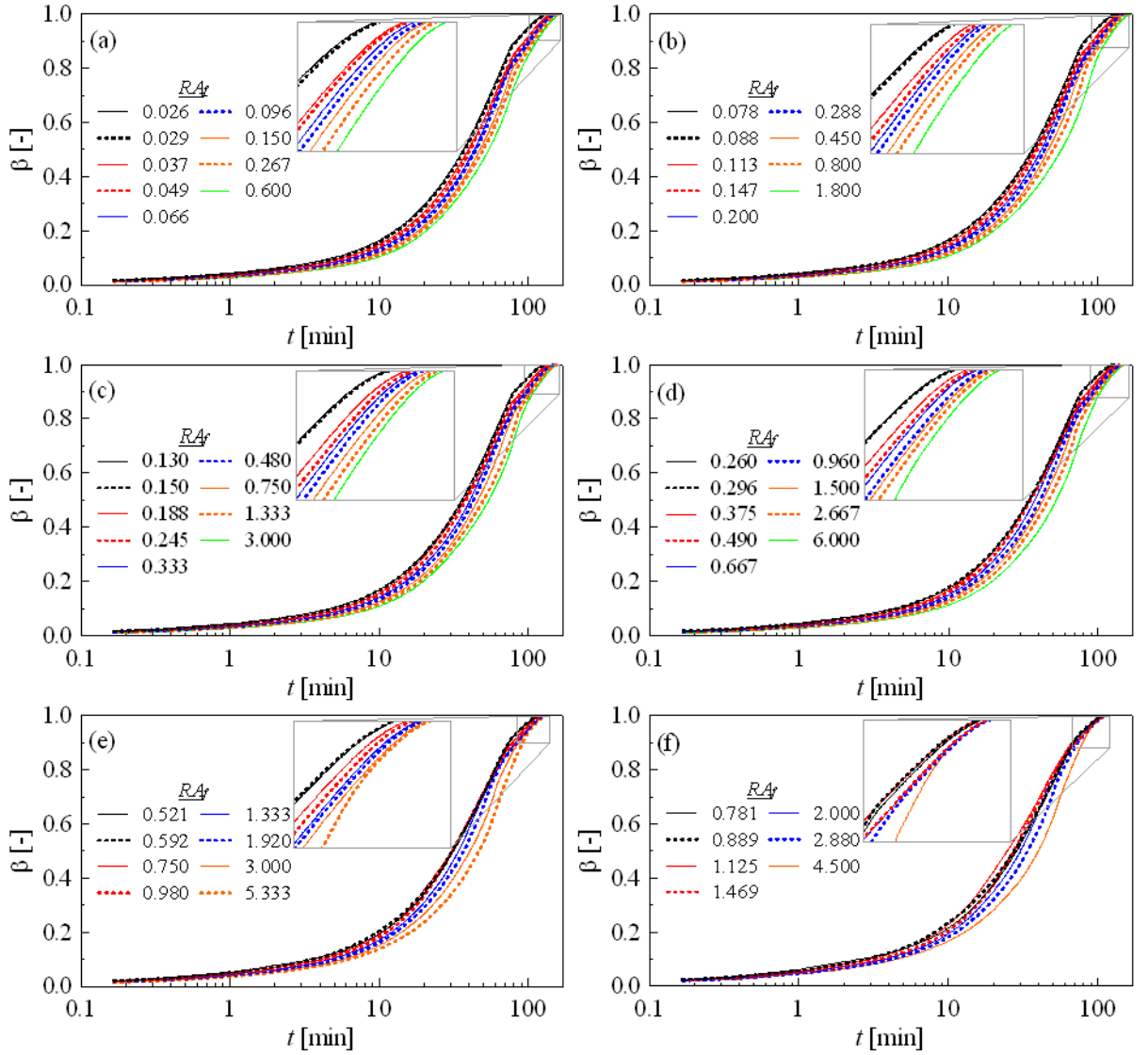


Figure 10 –  $\beta$  vs.  $t$  for several values of  $RA_f$  and: (a)  $\phi = 0.01$ ; (b)  $\phi = 0.03$ ; (c)  $\phi = 0.05$ ; (d)  $\phi = 0.1$ ; (e)  $\phi = 0.2$  and (f)  $\phi = 0.3$ .

A deeper understanding of how the total melting time is affected by the various parameters can be obtained from Fig. 11: it shows the maximum time of the melting process ( $\beta = 1$ ) as a function of  $RA_f$  for all the simulated values of  $\phi$  of all 78 configurations. It can be immediately observed that increases of  $\phi$  are associated with decreases in the time required for the PCM to completely melt. For example, at  $RA_f = 1$  and for  $\phi = 0.02$  and  $0.2$ , the maximum melting times were approximately 165 min and 127 min, respectively. Therefore, the increase of an order of magnitude in the  $\phi$  value led to a reduction of approximately 38 min in the melting process.

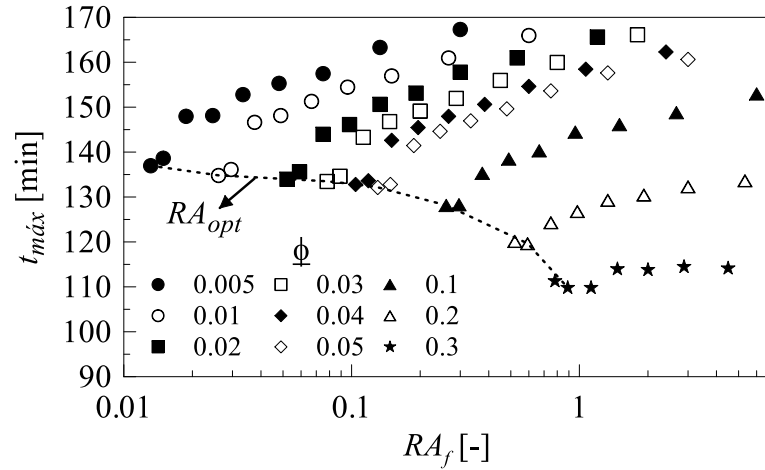


Figure 11 – Maximum melting time of each fin configuration as function of  $RA_f$  and several values of  $\phi$ .

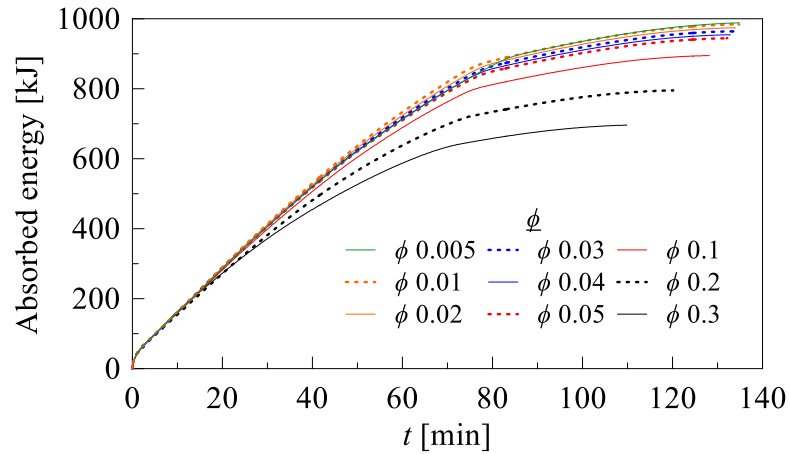
For this study the optimum aspect ratio ( $RA_{opt}$ ) was defined as the one with the lowest melting rate, i.e. the shortest time to reach complete melting for each  $\phi$ . For  $\phi$  ranging from 0.005 to 0.1, the shortest melting times were obtained with the lowest  $RA_f$ . However, for  $\phi = 0.2$  and 0.3, the shortest time occurred in the “second lowest”  $RA_f$ , which were designated the proper  $RA_{opt}$ . The total trend of the  $RA_{opt}$  values is plotted in Figure 12 as a dashed line. Similar behavior was observed for this configuration in other studies (Biserni, Rocha, and Bejan 2004) in which the optimal geometries proved to be the ones which permitted, as far as possible, the morphing “inverted fins” to penetrate the cavity. The optimal values of aspect ratios found in this study are shown in Table 5 with respect to tested values of  $\phi$ .

Table 5 -  $RA_{opt}$  at corresponding values of  $\phi$ .

$\phi$	0.005	0.01	0.02	0.03	0.04	0.05	0.1	0.2	0.3
$RA_{opt}$	0.013	0.026	0.052	0.078	0.104	0.130	0.260	0.592	0.889

Further work was conducted with the investigation of the absorbed energy. Since the cavity area ( $A_c$ ) was constant, the fin area ( $A_f$ ) obviously increased with increases of the area fraction ( $\phi = A_f/A_c$ ). Under these conditions, increasing  $\phi$  implied a reduction in the amount of mass contained in the cavity and the resulting variation in the energy absorbed by it. This behavior can be observed in Fig. 12, which shows the total energy absorbed by the cavity as a function of time for the optimal aspect ratios  $RA_{opt}$  with respect to all tested area fractions  $\phi$ . It can be noticed that, as  $\phi$  increases, there is a reduction in absorbed energy as predicted. For example, between  $\phi = 0.1$  and  $\phi = 0.3$  at  $t = 100$  min, the energy absorbed is approximately 861 kJ and 690 kJ, respectively. This represents a reduction of around 20% in terms of absorbed energy. However, for a variation of 10% in area fraction

462 ( $\phi = 0.005$  and  $\phi = 0.05$ ) at  $t = 100$  min, the absorbed energy is around 935 kJ and 902 kJ, respectively.  
 463 These values represent a decrease of only approximately 3% of absorbed energy. Based on these  
 464 results, it can be concluded that the reduction of the absorbed energy should be significant only for  
 465 values of  $\phi$  greater than a threshold value of 0.05.



466

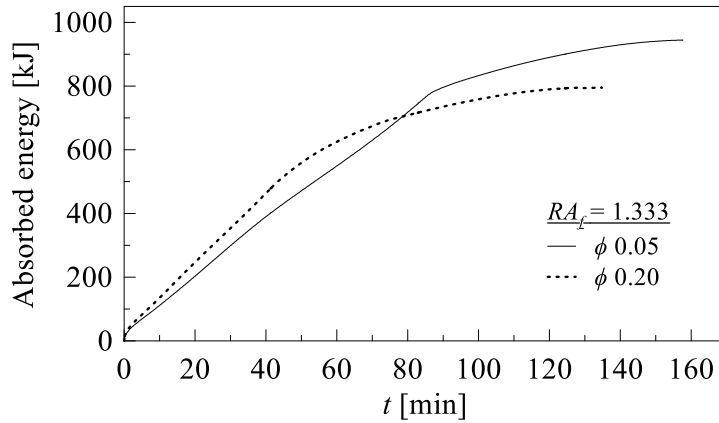
467 Figure 12 – Cavity absorbed energy over time with respect to the optimal aspect ratios,  $RA_{opt}$  and several  $\phi$   
 468 values.

469 Finally, Fig. 13 shows the variation of the energy absorbed in the cavity as a function of time  
 470 with respect to the cases  $RA_f = 1.33$  and  $\phi = 0.05$  and 0.2. Figure 13 shows a clear inversion in trend  
 471 at a time of approximately 80 min. For times shorter than 80 min, an increase in  $\phi$  results in an increase  
 472 in absorbed energy. For example, at  $t = 60$  min and  $\phi = 0.05$  and  $\phi = 0.2$ , approximately 549 kJ and  
 473 625 kJ were absorbed, respectively. This represents an increase of 12% in absorbed energy when  $\phi$  is  
 474 increased from 0.05 to 0.2. This behavior may be of great interest in applications that require a high  
 475 storage rate in shorter times. In contrast, for times longer than 80 min, the opposite behavior is  
 476 observed with a decrease in  $\phi$  resulting in an increase in absorbed energy. For example, at  $t = 120$   
 477 min, for  $\phi = 0.05$  and 0.2, approximately 890 kJ and 790 kJ were absorbed, respectively. This  
 478 demonstrates that a 15% increase in area fraction resulted in approximately an 11% reduction in total  
 479 energy absorption.

480



Figure 13 – Absorbed energy over time for  $RA_f = 1.33$  and  $\phi = 0.05$  and  $0.2$ .



## 5. Conclusions

The present work was concerned with the effect of the aspect ratio of an “inverted fin”, i.e. an intrusion placed in a rectangular cavity, in the melting process of lauric acid PCM. Results were obtained by means of a computational model based on the equations of conservation of mass, momentum, energy and an enthalpy-porosity model representing the PCM melting process. The main conclusions were:

- a shear region between two convective currents was observed. This was a result of a buoyant upward flow in the region above the fin and a downward flow at the solid-liquid interface. Another region with great recirculation was observed between the base of the cavity and the base of the fin. In addition, the existing circulation along the top of the fin was classified as Rayleigh-Bénard convection.
- for all tested values of area fraction ( $\phi$ ), there was a reduction in total time of the melting process with a reduction of the value of the fin aspect ratio  $RA_f$ , caused by the increase of the fin width  $W_f$ . It was also noted that at  $t = 50$  min for  $\phi$  ranging from 0.01 to 0.05, with different values of  $RA_f$ , the solid-liquid interface profiles were similar to each other, differing only in the region to the left of the fin between  $W_f = 20$  mm and  $W_f = 48$  mm.
- $Nu$  profiles as a function of  $Fo$  for different  $RA_f$  and  $\phi = 0.01, 0.03, 0.05, 0.1, 0.2$  and  $0.3$  showed 3 distinct regions. Region I presented a marked reduction of  $Nu$  in the initial moments (mostly due to conduction). Region II presented  $Nu$  values without large variations but with fluctuations in most of the melting process (mostly due to convection). Region III presented sharp reductions of  $Nu$  in the final moments, due to the weakening of convection currents.
- The various parameters affecting the total melting time were investigated with reference to the 78 simulated configurations. The increase of  $\phi$  was associated with decreasing times required

for the PCM to completely melt. For example, for  $RA_f = 1$  and  $\phi = 0.02$  and  $0.2$ , the maximum melting times were approximately 165 min and 127 min, respectively. Therefore, the increase of an order of magnitude in the value of  $\phi$  led to a reduction of approximately 38 min in the melting process.

- Finally, an investigation regarding the amount of absorbed energy with respect to  $RA_{opt}$  was carried out. It was noticed that there was a reduction in absorbed energy as  $\phi$  increased. For example, at  $t = 100$  min for  $\phi = 0.1$  and  $\phi = 0.3$ , the energy absorbed was approximately 861 kJ and 690 kJ, respectively. This represented a reduction of around 20% in terms of absorbed energy. However, for an increase of 10% of area fraction ( $\phi = 0.005$  to  $\phi = 0.05$ ) at  $t = 100$  min, the absorbed energy was around 935 kJ and 902 kJ, respectively. These values represented a decrease of 3% of absorbed energy. With these results, it was concluded that the reduction of the absorbed energy was significant only for  $\phi$  greater than a threshold value of 0.05.

## Acknowledgments

This work was supported by UNISINOS (University of Vale do Rio dos Sinos), CAPES (Coordination for the Improvement of Higher Education Personnel) and FAPERGS (Research Support Foundation of the State of Rio Grande do Sul). Financial support was provided by CAPES (Coordination for the Improvement of Higher Education Personnel) – Grant Financing Code 001. Author C. Biserni was sponsored by the Italian Ministry for Education, University and Research.

## References

- Abdulateef, Ammar M., Sohif Mat, Kamaruzzaman Sopian, Jasim Abdulateef, and Ali A. Gitan. 2017. "Experimental and Computational Study of Melting Phase-Change Material in a Triplex Tube Heat Exchanger with Longitudinal/Triangular Fins." *Solar Energy* 155: 142–53. <https://doi.org/10.1016/j.solener.2017.06.024>.
- Agyenim, Francis, Neil Hewitt, Philip Eames, and Mervyn Smyth. 2010. "A Review of Materials, Heat Transfer and Phase Change Problem Formulation for Latent Heat Thermal Energy Storage Systems (LHTESS)." *Renewable and Sustainable Energy Reviews* 14 (2): 615–28. <https://doi.org/10.1016/j.rser.2009.10.015>.
- Akeiber, Hussein, Payam Nejat, Muhd Zaimi Abd Majid, Mazlan A. Wahid, Fatemeh Jomehzadeh, Iman Zeynali Famileh, John Kaiser Calautit, Ben Richard Hughes, and Sheikh Ahmad Zaki. 2016. "A Review on Phase Change Material (PCM) for Sustainable Passive Cooling in Building Envelopes." *Renewable and Sustainable Energy Reviews* 60: 1470–97. <https://doi.org/10.1016/j.rser.2016.03.036>.
- Arshad, Adeel, Mark Jabbal, Pouyan Talebizadeh Sardari, Muhammad Anser Bashir, Hamza Faraji, and

538 Yuying Yan. 2020. "Transient Simulation of Finned Heat Sinks Embedded with PCM for Electronics  
 539 Cooling." *Thermal Science and Engineering Progress* 18 (August).  
 540 <https://doi.org/10.1016/j.tsep.2020.100520>.

541 Aslfattahi, Navid, R. Saidur, Mohd Faizul Mohd Sabri, and A. Arifutzzaman. 2019. "Experimental  
 542 Investigation of Thermal Stability and Enthalpy of Eutectic Alkali Metal Solar Dispersed with MGO  
 543 Nanoparticles." *International Journal of Technology* 10 (6): 1112-1119.  
 544 <https://dx.doi.org/10.14716/ijtech.v10i6.3568>.

545 Aslfattahi, Navid, R. Saidur, A. Arifutzzaman, R. Sadri, Nuno Bimbo, Mohd Faizul Mohd Sabri, Philip A  
 546 Maughan, Luc Bouscarrat, Richard J. Dawson, Suhana Mohd Said, Boon Tong Goh, and Nor Azwadi  
 547 Che Sidik. 2020. "Experimental investigation of energy storage properties and thermal conductivity of  
 548 a novel organic phase change material/MXene as A new class of nanocomposites." *Journal of Energy  
 549 Storage* 27: 101115. <https://doi.org/10.1016/j.est.2019.101115>.

550 Baby, Rajesh, and C. Balaji. 2012. "Experimental Investigations on Phase Change Material Based Finned  
 551 Heat Sinks for Electronic Equipment Cooling." *International Journal of Heat and Mass Transfer* 55  
 552 (5–6): 1642–49. <https://doi.org/10.1016/j.ijheatmasstransfer.2011.11.020>.

553 Biserni, C., L. A.O. Rocha, and A. Bejan. 2004. "Inverted Fins: Geometric Optimization of the Intrusion into  
 554 a Conducting Wall." *International Journal of Heat and Mass Transfer* 47 (12–13): 2577–86.  
 555 <https://doi.org/10.1016/j.ijheatmasstransfer.2003.12.018>.

556 Celik, Ismail B., Urmila Ghia, Patrick J. Roache, Christopher J. Freitas, Hugh Coleman, and Peter E. Raad.  
 557 2008. "Procedure for Estimation and Reporting of Uncertainty Due to Discretization in CFD  
 558 Applications." *Journal of Fluids Engineering, Transactions of the ASME* 130 (7): 0780011–14.  
 559 <https://doi.org/10.1115/1.2960953>.

560 Chuah, T.G., D. Rozanna, A. Salmiah, S. Y. Thomas Choong, and M. Sa'ari. 2006. "Fatty Acids Used as  
 561 Phase Change Materials ( PCMs ) for Thermal Energy Storage in Building Material Applications."  
 562 *Applied Energy*, no. July: 123–37.

563 Dabiri, Soroush, Mehdi Mehrpooya, and Erfan Ghavami Nezhad. 2018. "Latent and Sensible Heat Analysis  
 564 of PCM Incorporated in a Brick for Cold and Hot Climatic Conditions, Utilizing Computational Fluid  
 565 Dynamics." *Energy* 159: 160–71. <https://doi.org/10.1016/j.energy.2018.06.074>.

566 Ehms, José Henrique Nazzi, Rejane De Césaró Oliveski, Luiz Alberto Oliveira Rocha, Cesare Biserni, and  
 567 Massimo Garai. 2019. "Fixed Grid Numerical Models for Solidification and Melting of Phase Change  
 568 Materials (PCMs)." *Applied Sciences* 9: 4334. <https://doi.org/10.3390/app9204334>.

569 Hasnain, S M. 1998. "Review on Sustainable Thermal Energy Storage Technologies, Part I: Heat Storage  
 570 Materials and Techniques." *Energy Conversion and Management* 39 (11): 1127–38.

571 Ibrahim, Nasiru I., Fahad A. Al-Sulaiman, Saidur Rahman, Bekir S. Yilbas, and Ahmet Z. Sahin. 2017.  
 572 "Heat Transfer Enhancement of Phase Change Materials for Thermal Energy Storage Applications: A  
 573 Critical Review." *Renewable and Sustainable Energy Reviews* 74: 26–50.

574 <https://doi.org/10.1016/j.rser.2017.01.169>.

575 Jaguemont, Joris, Noshin Omar, Peter Van den Bossche, and Joeri Mierlo. 2018. "Phase-Change Materials  
576 (PCM) for Automotive Applications: A Review." *Applied Thermal Engineering* 132: 308–20.  
577 <https://doi.org/10.1016/j.applthermaleng.2017.12.097>.

578 Jamil, Nurfatihah, Jesbains Kaur, Ak. Pandey, Syed Shahabuddin, Samir Hassani, Rahman Saidur,  
579 Roshafima Rasit Ali, Nor Azwadi Che Sidik, and Mohd Naim. 2019. "A Review on Nano Enhanced  
580 Phase Change Materials: An Enhancement in Thermal Properties and Specific Heat Capacity." *Journal  
581 of Advanced Research in Fluid Mechanics and Thermal Sciences* 57: 110-120.

582 Ji, Chenzhen, Zhen Qin, Swapnil Dubey, Fook Hoong Choo, and Fei Duan. 2018. "Simulation on PCM  
583 Melting Enhancement with Double-Fin Length Arrangements in a Rectangular Enclosure Induced by  
584 Natural Convection." *International Journal of Heat and Mass Transfer* 127: 255–65.  
585 <https://doi.org/10.1016/j.ijheatmasstransfer.2018.07.118>.

586 Joshi, Varun, and Manish K. Rathod. 2019. "Constructal Enhancement of Thermal Transport in Latent Heat  
587 Storage Systems Assisted with Fins." *International Journal of Thermal Sciences* 145 (November).  
588 <https://doi.org/10.1016/j.ijthermalsci.2019.105984>.

589 Kalbasi, Rasool, and Mohammad Reza Salimpour. 2015. "Constructal Design of Horizontal Fins to Improve  
590 the Performance of Phase Change Material Rectangular Enclosures." *Applied Thermal Engineering* 91:  
591 234–44. <https://doi.org/10.1016/j.applthermaleng.2015.08.024>.

592 Kalnaes, Simen Edsjo, Bjorn Petter Jelle. 2015. "Phase change materials and products for building  
593 applications: A state-of-the-art review and future research opportunities." *Energy and Buildings* 94:  
594 150-176. <https://dx.doi.org/10.1016/j.enbuild.2015.02.023>.

595 Kamkari, Babak, and Hossein Shokouhmand. 2014. "Experimental Investigation of Phase Change Material  
596 Melting in Rectangular Enclosures with Horizontal Partial Fins." *International Journal of Heat and  
597 Mass Transfer* 78: 839–51. <https://doi.org/10.1016/j.ijheatmasstransfer.2014.07.056>.

598 Kazemi, M., M. J. Hosseini, A. A. Ranjbar, and R. Bahrapoury. 2018. "Improvement of Longitudinal Fins  
599 Configuration in Latent Heat Storage Systems." *Renewable Energy* 116: 447–57.  
600 <https://doi.org/10.1016/j.renene.2017.10.006>.

601 Khan, Mohammed Mumtaz A., R. Saidur, Fahad A. Al-Sulaiman. 2017. "A review for phase change  
602 materials (PCMs) in solar absorption refrigeration systems." *Renewable and Sustainable Energy  
603 Reviews* 76: 105-137. <https://doi.org/10.1016/j.rser.2017.03.070>.

604 Kok, Besir. 2020. "Examining Effects of Special Heat Transfer Fins Designed for the Melting Process of  
605 PCM and Nano-PCM." *Applied Thermal Engineering* 170 (April).  
606 <https://doi.org/10.1016/j.applthermaleng.2020.114989>.

607 Leducq, D., F. T. NDoye, G. Alvarez. 2015. "Phase change material for the thermal protection of ice cream  
608 during storage and transportation." *International Journal of Refrigeration* 52: 133-139.  
609 <http://dx.doi.org/10.1016/j.ijrefrig.2014.08.012>.

Mostafavi, Amirhossein, Mohammad Parhizi, and Ankur Jain. 2019. "Theoretical Modeling and Optimization of Fin-Based Enhancement of Heat Transfer into a Phase Change Material." *International Journal of Heat and Mass Transfer* 145 (December).  
<https://doi.org/10.1016/j.ijheatmasstransfer.2019.118698>.

Pielichowska, Kinga, and Krzysztof Pielichowski. 2014. "Phase Change Materials for Thermal Energy Storage." *Progress in Materials Science* 65: 67–123. <https://doi.org/10.1016/j.pmatsci.2014.03.005>.

Pizzolato, Alberto, Ashesh Sharma, Kurt Maute, Adriano Sciacovelli, and Vittorio Verda. 2017. "Design of Effective Fins for Fast PCM Melting and Solidification in Shell-and-Tube Latent Heat Thermal Energy Storage through Topology Optimization." *Applied Energy* 208 (October): 210–27.  
<https://doi.org/10.1016/j.apenergy.2017.10.050>.

Pu, Liang, Shengqi Zhang, Lingling Xu, and Yanzhong Li. 2020. "Thermal Performance Optimization and Evaluation of a Radial Finned Shell-and-Tube Latent Heat Thermal Energy Storage Unit." *Applied Thermal Engineering* 166 (November 2019): 114753.  
<https://doi.org/10.1016/j.applthermaleng.2019.114753>.

Reddy, K. S., Vijay Mudgal, and T. K. Mallick. 2018. "Review of Latent Heat Thermal Energy Storage for Improved Material Stability and Effective Load Management." *Journal of Energy Storage* 15: 205–27.  
<https://doi.org/10.1016/j.est.2017.11.005>.

Shokouhmand, Hossein, and Babak Kamkari. 2013. "Experimental Investigation on Melting Heat Transfer Characteristics of Lauric Acid in a Rectangular Thermal Storage Unit." *Experimental Thermal and Fluid Science* 50: 201–12. <https://doi.org/10.1016/j.expthermflusci.2013.06.010>.

Souayfane, Farah, Farouk Fardoun, Pascal-Henry Biwolé. 2016. "Phase change materials (PCM) for cooling applications in buildings: A review." *Energy and Buildings* 129: 396–431.  
<http://dx.doi.org/10.1016/j.enbuild.2016.04.006>.

Sun, Kun, Huan Liu, Xiaodong Wang, and Dezhen Wu. 2019. "Innovative Design of Superhydrophobic Thermal Energy-Storage Materials by Microencapsulation of n-Docosane with Nanostructured ZnO/SiO<sub>2</sub> Shell." *Applied Energy* 237 (January): 549–65.  
<https://doi.org/10.1016/j.apenergy.2019.01.043>.

Valeri, Daniella, and Antonio J.A. Meirelles. 1997. "Viscosities of Fatty Acids, Triglycerides, and Their Binary Mixtures." *JAACS, Journal of the American Oil Chemists' Society* 74 (10): 1221–26.  
<https://doi.org/10.1007/s11746-997-0048-6>.

Voller, V. R., and C. Prakash. 1987. "A Fixed Grid Numerical Modelling Methodology for Convection-Diffusion Mushy Region Phase-Change Problems." *International Journal of Heat and Mass Transfer* 30 (8): 1709–19. [https://doi.org/10.1016/0017-9310\(87\)90317-6](https://doi.org/10.1016/0017-9310(87)90317-6).

Wu, Shaofei, Ting Yan, Zihan Kuai, and Weiguo Pan. 2020. "Thermal Conductivity Enhancement on Phase Change Materials for Thermal Energy Storage: A Review." *Energy Storage Materials* 25 (September 2019): 251–95. <https://doi.org/10.1016/j.ensm.2019.10.010>.

646 Zhang, Huili, Jan Baeyens, Gustavo Cáceres, Jan Degreè, and Yongqin Lv. 2016. “Thermal Energy  
647 Storage: Recent Developments and Practical Aspects.” *Progress in Energy and Combustion Science*  
648 53: 1–40. <https://doi.org/10.1016/j.pecs.2015.10.003>.

649 Zhang, Xuelai, Xudong Chen, Zhong Han, and Weiwen Xu. 2016. “Study on Phase Change Interface for  
650 Erythritol with Nano-Copper in Spherical Container during Heat Transport.” *International Journal of*  
651 *Heat and Mass Transfer* 92: 490–96. <https://doi.org/10.1016/j.ijheatmasstransfer.2015.08.095>.

652 Zhu, Na, Zhenjun Ma, and Shengwei Wang. 2009. “Dynamic Characteristics and Energy Performance of  
653 Buildings Using Phase Change Materials: A Review.” *Energy Conversion and Management* 50 (12):  
654 3169–81. <https://doi.org/10.1016/j.enconman.2009.08.019>.

655

656